A modeling study of lifetime and performance improvements of solid oxide fuel cell by reversed pulse operation

Rizvandi, Omid Babaie; Jensen, Søren Højgaard; Frandsen, Henrik Lund

Published in:
Journal of Power Sources

DOI (link to publication from Publisher):
10.1016/j.jpowsour.2022.231048

Publication date:
2022

Document Version
Publisher's PDF, also known as Version of record

Journal of Power Sources 523 (2022) 231048

Contents lists available at ScienceDirect

Journal of Power Sources

journal homepage: www.elsevier.com/locate/jpowsour

A modeling study of lifetime and performance improvements of solid oxide fuel cell by reversed pulse operation

Omid Babaie Rizvandi [a,*], Søren Højgaard Jensen [b,c], Henrik Lund Frandsen [a]

[a] Department of Energy Conversion and Storage, Technical University of Denmark (DTU), Building 310, Fysikvej, DK-2800 Lyngby, Denmark
[b] Department of Energy Technology, Aalborg University, 9220, Aalborg Øst, Denmark
[c] DynElectro ApS, 4130, Viby Sjælland, Denmark

HIGHLIGHTS

- Numerical investigation of benefits of co-production operation of SOCs.
- SOC lifetime and performance improvements by reversed pulse operation.
- Alleviation of chromium poisoning.
- Cyclic operation with longer electrolysis mode improve SOC lifetime and performance.
- Mild electrolysis starting from the beginning enhance SOC lifetime and performance.

ARTICLE INFO

Keywords:
Solid oxide cell
Chromium poisoning
Reversed pulse operation
Degradation
Lifetime
Performance

1 ABSTRACT

Chromium poisoning of the air electrode is a primary degradation mechanism for solid oxide cells (SOCs) operating under fuel cell mode. Recent experimental findings show that reversed pulse operation for SOCs operated as electrolyser cells can reverse this degradation and extend the lifetime. Here, we use a multiphysics model of an SOC to investigate the effects of reversed pulse operation for alleviating chromium poisoning of the air electrode. We study the effects of time fraction of the operation under fuel cell and electrolysis modes, cyclic operation starting after a certain duration, and fuel cell and electrolysis current densities on the cell lifetime, total power, and hydrogen production. Our modeling shows that reversed pulse operation enhances cell lifetime and total power for all different cases considered in this study. Moreover, results suggest that the cell lifetime, total power, and hydrogen production can be increased by reversed pulse operation at longer operation times under electrolysis mode, cyclic operation starting from the beginning, and lower electrolysis current densities. All in all, this paper documents and establishes a computational framework that can serve as a platform to assess and quantify the increased profitability of SOCs operating under a co-production operation through reversed pulse operation.

1. Introduction

SOCs are among the most promising energy conversion devices due to their high efficiency and fuel flexibility owing to their high operating temperature. Another important advantage of SOCs is their dual function of operating in both fuel cell (SOFC) and electrolysis (SOEC) modes by converting the chemical energy of the reactants to electricity and vice versa. However, the degradation of SOCs due to different physical phenomena, especially under higher current densities, is an important issue that needs to be improved for their further commercialization.

Major degradation phenomena should be investigated to develop proper mechanisms for them and so searching adequate mitigation techniques for their reduction to improve SOCs lifetime. An extensive number of studies have been devoted to the investigation of the degradation phenomena occurring under SOFC and SOEC operation modes; dozens of them can be found in the review articles [1–6]. The main degradation phenomena under the SOFC operation mode are the chromium (Cr) poisoning of the air electrode [7,8] and nickel (Ni) coarsening in the fuel electrode [9,10], while Ni migration and air electrode delamination are the dominant degradation mechanisms under the SOEC operation mode [11,12]. In addition, corrosion of the metallic

* Corresponding author.
E-mail address: obari@dtu.dk (O.B. Rizvandi).

https://doi.org/10.1016/j.jpowsour.2022.231048
Received 8 October 2021; Received in revised form 14 January 2022; Accepted 18 January 2022
Available online 29 January 2022

Nomenclature

Abbreviation

ASR	Area-specific-resistance
BV	Butler-Volmer
Cr	Chromium
DOF	Number of degrees of freedom
EOL	End-of-life
FEM	Finite element method
IC	Interconnect
Ni	Nickel
OCV	Open-circuit voltage
SOEC	Solid oxide electrolysis cell
SOFC	Solid oxide fuel cell
SOC	Solid oxide cell
TPB	Triple-phase boundary
TSO	Transmission service operator
nfb	Cyclic operation not conducted from the beginning of the cell lifetime

Symbols

A	Surface area
c_p	Heat capacity at constant pressure
D	Diffusion coefficient, remanent electric displacement
d	Depth
E	Open-circuit voltage, activation energy
F	Faraday's constant
G	Gibbs free energy
h	Height
k	Thermal conductivity, turbulence kinetic energy
k_B	Boltzmann constant
I	Current
i	Reaction rate
J	Current density
M	Molecular weight
n	Mole number
p	Pressure
R	Universal gas constant
r	Radius
T	Temperature
t	Time
S	Source term
u	Velocity
V	Voltage
w	Mass fraction
x	Mole fraction

Greek letters

∇	Vector differential operator
η	Overpotential, utilization
λ	Effective volumetric TPB length
σ	Conductivity
ρ	Density
ε	Porosity, permittivity
ψ	Volume fraction
ω	Specific rate of dissipation of the kinetic energy
γ	Surface energy of Ni
Ω	Diffusion volume element of Ni
δ_S	Inter-atomic spacing of Ni
θ	Contact angle

Subscripts and superscripts

act	Activation
an	Anode
ca	Cathode
conc	Concentration
Cr	Chromium
el	Electrolysis
eq	Equivalent
IC	Interconnect
in	Inlet
Ni	Nickel
ohm	Ohmic
out	Outlet
ox	Oxidation

interconnect (IC) [13,14] occurs under both operation modes.

Cr poisoning is the prominent degradation phenomenon for the SOC operating under the fuel cell model (SOFC), especially at lower operating temperatures [15,17]. Cr poisoning is reasonably well understood and described in the literature [15–17]. It occurs at the reaction sites on the air electrode due to the deposition of the volatile Cr-species from the IC and upstream metal piping, which is carried in the air flow. Experiments [18–20] demonstrated that Cr distributes uniformly over the air electrode under the open-circuit voltage (OCV), while Cr contents are located close to the active part of the air electrode under load currents, and Cr deposition increases with increasing current density (overpotential). Nakajo et al. [21] proposed a Cr poisoning model determining the reduction of the air electrode triple-phase boundary (TPB) as a function of Cr oxidation reaction rate at the TPBs. Several mitigation techniques for Cr poisoning have been proposed in the literature, e.g. improving the materials used for the air electrode [22] and coating the IC [23].

Recent experimental studies have shown the alleviating effects of the reverse operation of the SOC on the degradation phenomena occurring under each operation mode (SOFC/SOEC) [26–29]. The dual-functioning capability of the SOCs, i.e. generating/consuming power by operating under the fuel cell/electrolysis mode, makes them adequate candidates to regulate the fluctuations in renewable energies such as solar and wind. Therefore, reversible SOCs can be considered to act as batteries, where massive amounts of energy can be stored with moderate round-trip efficiency [24,25].

Hughes et al. [26] performed up to 1000 h of SOCs durability tests under constant current and reversible cyclic currents with cycle periods of 1 and 12 h and half of the cycles under each operation mode. The authors showed that reversible operation of the SOC did not cause any new degradation phenomena. Moreover, it was shown that the reversible cyclic operation reduced the degradation of the cell compared to the constant current case, and applying more frequent cycles further slows down the degradation rate.

Graves et al. [27] conducted 4000 h of reversible cyclic operation of a SOC and demonstrated that it could effectively alleviate the intense degradation of the cell under SOEC operation mode, i.e. delamination of the oxygen electrode, which was believed to be irreversible. The authors considered cyclic between SOEC and SOFC operation modes with load current densities of −1 and 0.5 A/cm^2 and durations of 1 and 5 h,

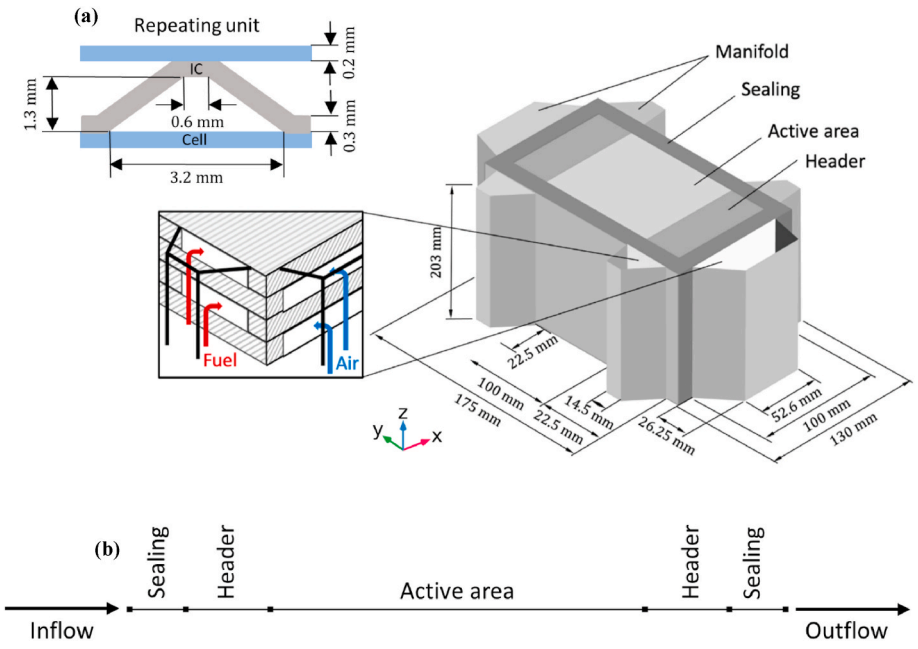

Fig. 1. Schematics of the modeling domains: (a) 3D model, adapted from Ref. [17], and (b) 1D model used in this study.

Table 1
Transport governing equations.

Description	Transport equation	Eq. #
Mass	$\frac{\partial(\varepsilon\rho)}{\partial t}+\nabla\cdot(\rho\mathbf{u})=S_{\mathrm{m}}$	(1)
Momentum	$\nabla p=\frac{\mu}{K}u_{av}$	(2)
Species	$\varepsilon\rho\frac{\partial w_{\mathrm{i}}}{\partial t}+\nabla\cdot\left(-\rho w_{\mathrm{i}}\sum_{j}D_{\mathrm{ij}}\nabla w_{\mathrm{j}}\right)+\rho(\mathbf{u}\cdot\nabla)w_{\mathrm{i}}=S_{\mathrm{i}}$	(3)
Heat	$(\rho c_p)_{\mathrm{eff}}\frac{\partial T}{\partial t}+(\rho c_p)_{\mathrm{eff}}\mathbf{u}\cdot\nabla T+\nabla\cdot(-k_{\mathrm{eff}}\nabla T)=S_{\mathrm{T}}$	(4)
Charge	$\nabla\cdot\left(-\sigma\nabla V+\frac{\partial D}{\partial t}+J_e\right)=S_{\mathrm{j}}\quad;\quad D=-\varepsilon_0\varepsilon_r\nabla V$	(5)

respectively.

Recently, Zhu et al. [28] employed an electrochemical cleaning approach to alleviating the Cr poisoning of the air electrode under the SOFC operation mode via reversing the operation to SOEC mode. The authors showed that operating the cell poisoned by Cr under a short SOEC operation mode can effectively remove most of the Cr content from the air electrode and recover a significant portion of the initial performance of the cell. They achieved 67% performance recovery for 2 h operation under SOEC mode after poisoning the cell under the SOFC mode for 120 h. A mild and short SOEC period was considered to avoid other degradation phenomena happening under SOEC operation mode. However, these degradations could be mitigated through operating under SOFC operation mode, as indicated in Ref. [27]. Besides Cr poisoning, Hauch et al. [29] showed that silicon poisoning occurring during SOEC operation could be alleviated by a brief SOFC operation.

In this study, we use a multiphysics model of a SOC, which has been developed for degradation analysis of an SOFC stack [17], to investigate the effects of the reversed pulse operation on alleviating Cr poisoning of the air electrode. We show how the Cr poisoning model, used in this study, captures the Cr cleaning of the air electrode. Effects of the time fraction of the operation under fuel cell and electrolysis modes, their current densities, and cyclic operation initiated after some time of operation are investigated. The results show that it is possible to achieve

Table 2
Cell model equations.

Description	Governing equation	Eq. #
Cell voltage [34]	$V_{cell}=E-\eta_{act,an}-\eta_{act,ca}-\eta_{conc,an}-\eta_{conc,ca}-\eta_{ohm}$	(6)
OCV [34]	$E=\frac{\Delta G_{rx,H_2O}}{2F}+\frac{RT}{2F}\ln\left(\frac{p_{H_2}p_{O_2}^{1/2}}{p_{H_2O}p_0^{1/2}}\right)$	(7)
BV for the anode reaction rate [35]	$i_{\mathrm{an}}=i_{0,\mathrm{an}}\lambda_{\mathrm{an,eff}}\left[\exp\left(\frac{2F}{RT}\eta_{\mathrm{act,an}}\right)-\exp\left(-\frac{F}{RT}\eta_{\mathrm{act,an}}\right)\right]$	(8)
BV for the cathode reaction rate [36]	$i_{\mathrm{ca}}=i_{0,\mathrm{ca}}\lambda_{\mathrm{ca}}\left[\exp\left(\frac{2F}{RT}\eta_{\mathrm{act,ca}}\right)-\exp\left(-\frac{2F}{RT}\eta_{\mathrm{act,ca}}\right)\right]$	(9)
Anode exchange current density [37]	$i_{0,\mathrm{an}}=31.4\,p_{\mathrm{H_2}}^{-0.03}\,p_{\mathrm{H_2O}}^{0.4}\exp\left(-\frac{18300}{T}\right)$	(10)
Cathode exchange current density [38]	$i_{0,\mathrm{ca}}=2.14\times10^5\,p_{\mathrm{O_2}}^{0.376}\exp\left(-\frac{29200}{T}\right)$	(11)
Anode concentration overpotential [39]	$\eta_{conc,an}=\frac{RT}{2F}\ln\left(\frac{1+\frac{RTh_{an}}{2FD^{eff}_{H_2O}p_{H_2O}}j}{1-\frac{RTL_{an}}{2FD^{eff}_{H_2}p_{H_2}}j}\right)$	(12)
Cathode concentration overpotential [39]	$\eta_{conc,ca}=\frac{RT}{4F}\ln\left(\frac{1}{1-\frac{RTh_{ca}}{4FD^{eff}_{O_2}p_{O_2}}j}\right)$	(13)
Ohmic overpotential [40]	$\eta_{ohm}=\frac{h_i}{\sigma_i}j$; $\begin{cases}\sigma_{Ni}=3.27\times10^6-1065.3T\\ \sigma_{LSM}=\frac{4.2\times10^7}{T}\exp\left(-\frac{1150}{T}\right)\\ \sigma_{YSZ}=6.25\times10^4\exp\left(-\frac{10300}{T}\right)\end{cases}$	(14)

Table 3
Geometric parameters.

Parameter	Value	Description
w_{stack}	0.1 m	Width of the stack
d_{stack}	0.1 m	Depth of the stack
$w_{sealing}$	0.015 m	Width of the sealing domain
N_{cell}	100	Number of the cells
h_{IC}	3×10^{-4} m	Height of the interconnect
$h_{Ni,f}$	2×10^{-4} m	Height of the Ni foam
h_{cl}	3×10^{-4} m	Height of the contact layer
h_{cell}	2×10^{-4} m	Height of the cell
h_{ch}	1.3×10^{-3} m	Height of the channel
w_{ch}	0.6×10^{-3} and 3.2×10^{-3} m	Widths of the bases of the channel

significantly higher total power and hydrogen output through the prolonged lifetime of the SOC stack operating under the reversed pulse operation compared to the base SOFC operation.

2. Methodology

2.1. Stack-scale model

A multiphysics model including transport equations of mass, momentum, species, charges, and heat is used in this study; this has been developed in our previous works [17,31,34]. In the model, a homogenization approach is applied to the layered domains of the stack, which solves for the effective modeling variables over an equivalent porous domain with effective modeling parameters and properties for each physics. The application of this approach to the active area of the stack was introduced in Ref. [30]. The additions of the headers, sealing, and manifolds to the model are presented in Refs. [17,31]; the 3D schematic of the stack is shown in Fig. 1a.

The homogenization approach that we have been using in our recent works, including the current study, is like the homogenization used for the electrodes of a single cell, in which the transport equations are solved over an equivalent domain with effective modeling variables instead of solving the equations on a detailed electrode geometry with all the phases and pores. Our homogenized stack model replaces the whole repeating unit with an equivalent domain. This approach has been used by several research groups, e.g. in Ref. [41] for an SOFC stack and [42] for a polymer electrolyte fuel cell stack, and European companies. In our recent work [17], we validated our stack-scale model against the experimental data for the 18-cell FZJ Mark-F SOFC stack [44] under stationary operation and showed that the degradation models results are consistent with the common degradation trends reported in the literature.

The transport governing equations that are solved at the stack scale to obtain the effective modeling variables are given in Table 1, and the cell model equations used to evaluate the polarization characteristics of the cells are listed in Table 2. The geometric parameters are given in Table 3.

Using the 3D model for the cyclic operation is not computationally feasible for the full lifetime of the stack because each pulsed cycle requires a couple of hours of computation - depending on the fuel cell and electrolysis operating conditions and their time fractions. Hence, a lifetime simulation of each cyclic operation with the 3D model would take several months of computation.

Therefore, an equivalent 1D model, sketched in Fig. 1b, has been developed based on the same homogenization approach. This model resolves each cycle in a few minutes, which depends on the lifetime regime, as it is faster at the beginning with a lower degradation rate and gets slower for the final cycles under the severe degradation regime. Thus, the 1D model makes the lifetime simulation of the cyclic operation feasible within a day or two.

Table 4
Degradation phenomena equations.

	Description	Governing equation	Eq. #
Ni coarsening [9]	Ni particle radius	$r_{Ni} = \left(\frac{5C}{\lambda}(1-e^{\lambda t}) + (r_{Ni}^0)^5\right)^{\frac{1}{5}}$	(15)
		$C = D_S \frac{\gamma \Omega \delta_S}{2k_B T} \frac{\beta}{(1-\beta^2)(1+\beta^2)^{0.5}(1+\beta)^3} \frac{\overline{Z}_0}{\psi_{Ni}/r_{Ni}^0 + \psi_{YSZ}/r_{YSZ}^0} \psi_{Ni}$	(16)
	Electronic conductivity of the anode	$\sigma_{e,an} = \sigma_{e,an}^0 \left[\frac{\psi_{Ni} - \psi_{Ni}^t}{1+\varphi/(1-\varphi) - \psi_{Ni}^t}\right]^2$	(17)
	Percolation threshold of Ni, ψ_{Ni}^t	$\frac{\psi_{Ni}^t/r_{Ni}}{\psi_{Ni}^t/r_{Ni} + (1-\psi_{Ni}^t)/r_{YSZ}} \overline{Z} = 1.764$	(18)
	Average particle coordination number	$\overline{Z} = Z_{YSZ,YSZ} \frac{\psi_{Ni}/r_{Ni} + \psi_{YSZ}/r_{YSZ}}{\psi_{YSZ}/r_{YSZ}}$	(19)
	TPB density of the anode electrode	$\lambda_{an} = 2\pi \min(r_{Ni}, r_{YSZ})(\sin\theta) \left(\frac{3(1-\varphi)\psi_{Ni}}{4\pi r_{Ni}^3}\right) \left(0.5\left(1 + \frac{r_{Ni}^2}{r_{YSZ}^2}\right) Z_{YSZ,YSZ}\right)$	(20)
	Effective TPB density of the anode electrode	$\lambda_{an,eff} = \lambda_{an}\, p_{YSZ} \left(1 - \left(\frac{3.764 - Z_{YSZ,YSZ}\frac{\psi_{Ni}/r_{Ni}}{\psi_{YSZ}/r_{YSZ}}}{2}\right)^{2.5}\right)^{0.4}$	(21)
		$p_{YSZ} = \left(1 - \left(\frac{3.764 - Z_{YSZ,YSZ}}{2}\right)^{2.5}\right)^{0.4}$	(22)
Cr poisoning [16]	Cr poisoning reaction	$2CrO_2(OH)_{2(g)} + 6e^- \rightarrow Cr_2O_{3(s)} + 2H_2O + 3O^{2-}$	(23)
	TPB density of the cathode electrode	$\frac{1}{\lambda_{ca}} \frac{\partial \lambda_{ca}}{\partial t} = -\frac{M_{Cr_2O_3}}{6F\rho_{Cr_2O_3} h_{TPB}} i_D$	(24)
	Reaction rate of the Cr oxidation	$i_D = i_{0,D}\, x_{CrO_2(OH)_2}^{0.5}\, x_{H_2O,Cr\ source}^{0.5} 2\sinh\left(\frac{F}{2RT}\eta_{ca}\right)$	(25)
IC oxidation [21]	Wagner's law for the oxide scale growth	$\frac{\partial h_{IC,ox}^2}{\partial t} = k_{m_g} \exp\left(\frac{E_{a,ox}}{RT}\right)$	(26)
	Conductivity of the oxide scale	$\sigma_{IC,ox} = k_{ox} \exp\left(-\frac{E_{el}}{RT}\right)$	(27)
	ASR of the oxide scale	$ASR_{IC,ox} = \frac{h_{IC,ox}}{\sigma_{IC,ox}}$	(28)

Table 5
Degradation models parameters.

Parameter	Value	Description
k_B	$1.38064852 \times 10^{-23}$ J K^{-1}	Boltzmann constant
γ	1.9 J m^{-2}	Surface energy of Ni [9]
Ω	10.9 Å^3	Diffusion volume element of Ni [9]
δ_S	2.5 Å	Inter-atomic spacing of Ni [9]
D_S	4.8×10^{-11} m^2 h^{-1}	Atomic surface diffusion coefficient [9]
λ	2.5×10^{-4} h^{-1}	Fitting parameter for Ni coarsening model. It is chosen arbitrarily based on the ranges used in [9,43]
β	0.8	Fitting parameter for Ni coarsening model [10]
r^0_{Ni}	0.542 μm	Initial radius of Ni particles [9]
r^0_{YSZ}	0.3 μm	Initial radius of YSZ particles [9]
ψ_{Ni}	0.4	Volume fraction of Ni [43]
ψ_{YSZ}	0.6	Volume fraction of YSZ [43]
$Z_{YSZ,YSZ}$	6	Coordination number between YSZ particles [9]
θ	15°	Contact angle between Ni and YSZ particles [9]
$M_{Cr_2O_3}$	151.99 g mol^{-1}	Molecular weight of chromium oxide
$\rho_{Cr_2O_3}$	5.22 g cm^{-3}	Density of chromium oxide
h_{TPB}	35 nm	Maximum height of chromium oxide [16]
$i_{0,D}$	6.74 A m^{-2}	Exchange current density for Cr oxidation [16]
$x_{CrO_2(OH)_2}$	10^{-8}	Mole fraction of $CrO_2(OH)_2$ in the cathode electrode [21]
$x_{H_2O,Cr\ source}$	10^{-2}	Water vapor mole fraction in the chromium source [21]
k_{m_s}	1.38×10^4 cm^2 h^{-1}	A constant for the weight gain rate of the oxide scale [21]
$E_{a,ox}$	286.6 kJ mol^{-1}	Activation energy of the oxide scale [21]
k_{ox}	0.458 S cm^{-1}	A constant for the conductivity of the oxide scale [21]
E_{el}	33.3 kJ mol^{-1}	Activation energy for σ_{ox} [21]
ρ_{IC}	7.75 g cm^{-3}	Density of the IC (Crofer22APU)
M_{IC}	54.97 g mol^{-1}	Molar mass of the IC (Crofer22APU)

The 1D model describes the stack in the flow direction and includes all the domains except the manifolds. In the 1D simplification, all the cells in the stack are assumed to experience the same boundary conditions, mimicking an "infinitely tall stack" with no difference amongst the cells in the height of the stack. The voltage applied is thus the same on all the cells, and heat transfer between the cells is zero as all cells develop the same heat (adiabatic condition). The model could be improved to a 2D or 3D stack model, but this will increase the runtime of even a computationally effective model to months, why this has been avoided for the time being.

2.2. Degradation sub-models

The specific sub-models for the degradation phenomena of Ni particle coarsening in the anode electrode, Cr poisoning of the air electrode, and oxidation of the IC have already been reported in Ref. [17]. The degradation models equations and their parameters are given in Tables 4 and 5, respectively. Ni coarsening is defined analytically, Eq. (15), based on the Ostwald ripening mechanism [9], and the oxide scale growth over the IC is determined by Wagner's law [21], Eq. (26). The Cr poisoning model is described in more detail in the following for a clearer interpretation of the results.

Several studies, e.g. Refs. [16,18–20], have proposed the following mechanisms for the Cr poisoning of the air electrode: 1) an electrochemical reaction, Eq. (23), which indicates the oxidation of the volatile Cr species occurring at the TPBs of the air electrode and so reduces the TPBs; and 2) chemical reactions that replace the manganese atoms of the LSM crystal with the chromium and form phases such as SrCrO4. It has been shown that the Cr poisoning of the air electrode mainly occurs through the electrochemical reaction since higher Cr poisoning was observed for higher overpotentials [16]. Therefore, in this study, just the electrochemical reaction is considered for the Cr poisoning. Nakajo et al. [21] proposed the empirical relation (24) for the reduction of the TPBs of the LSM/YSZ electrode, which is defined as a function of the reaction rate of the Cr oxidation, i_D, determined by equation (25) as a function of the overpotential.

2.3. Operating conditions

The cyclic operation is applied to the model via rectangular pulses of the load current density cycling between fuel cell and electrolysis operation modes, as shown in Fig. 2a for the first 1000 h of the operation. In this graph, the cell is operated 95 and 5% of the time under fuel cell and electrolysis modes, respectively; onwards, this will be abbreviated as 95%–5%. Fig. 2b shows the initial evolution of the cell voltage corresponding to the load current density pulses given in Fig. 2a.

Smoothing with a transition time with a duration of 50% of the electrolysis operation time for each cyclic operation, as shown in Fig. 2c, is used to minimize the convergence difficulties and improve the runtime of the model. The effects of the transition time are investigated for the cyclic operation with 20% operation time under the electrolysis mode; the comparison is given in the Supplementary material. It is found that lower transition time, which leads to a longer operation time under electrolysis mode, results in longer lifetime and higher power and hydrogen production. Transition times of 25 and 75% of the electrolysis operation time vary the lifetime, total power, and hydrogen production by about 3, 4, and 8%, respectively, compared to the base transition time of 50% of the electrolysis operation time. In this study, we use the transition time of 50% of the electrolysis operation time since it is the shortest transition time that leads to a proper convergence for all the cyclic operations, especially the cyclic operation with the shortest electrolysis operation time, i.e. 5% operation time under electrolysis mode.

Inlets and outlets are located at the left and right edges of the modeling domain for both the fuel and air flows, respectively, which results in a co-flow configuration. Pressure boundary conditions are applied to the inlets and outlets, and the latter is atmospheric pressure. Moreover, the operating temperature is controlled by the gas inlet temperatures. The operating conditions are listed in Table 6. A detailed discussion of the modeling approach and geometric and modeling parameters can be found in Refs. [17,30,31].

The end-of-life (EOL) of the cell is defined at a drop of 20% of the SOFC operating voltage compared to the initial operating voltage. Up to this point, all the degradation regimes, including the final accelerated one, are captured with the current model. Because of the final severe degradation rate, the model is getting into convergence issues and crashing after resolving a portion of this regime.

2.4. Solution method

The software COMSOL Multiphysics is used to couple the governing equations and solve them numerically via the finite element method (FEM) approach. A mesh size of 1 mm is applied to all domains with 5 times denser mesh at the inlet and outlet of the active area, which leads to a number of degrees of freedom (DOF) of 1919. To ensure the mesh-independency of the results, the model is run for the base SOFC degradation with a refined mesh 5 times denser than the base mesh, i.e. the mesh size of 0.2 mm. The relative errors between the models voltage and maximums of the temperature and current density are within 0.02%, 0.002%, and 0.04%, respectively. The model is run on a high-end workstation with an Intel Core i9 3.5 GHz 12-core processor.

3. Results

Fig. 3 shows the base case with evolutions of various modeling

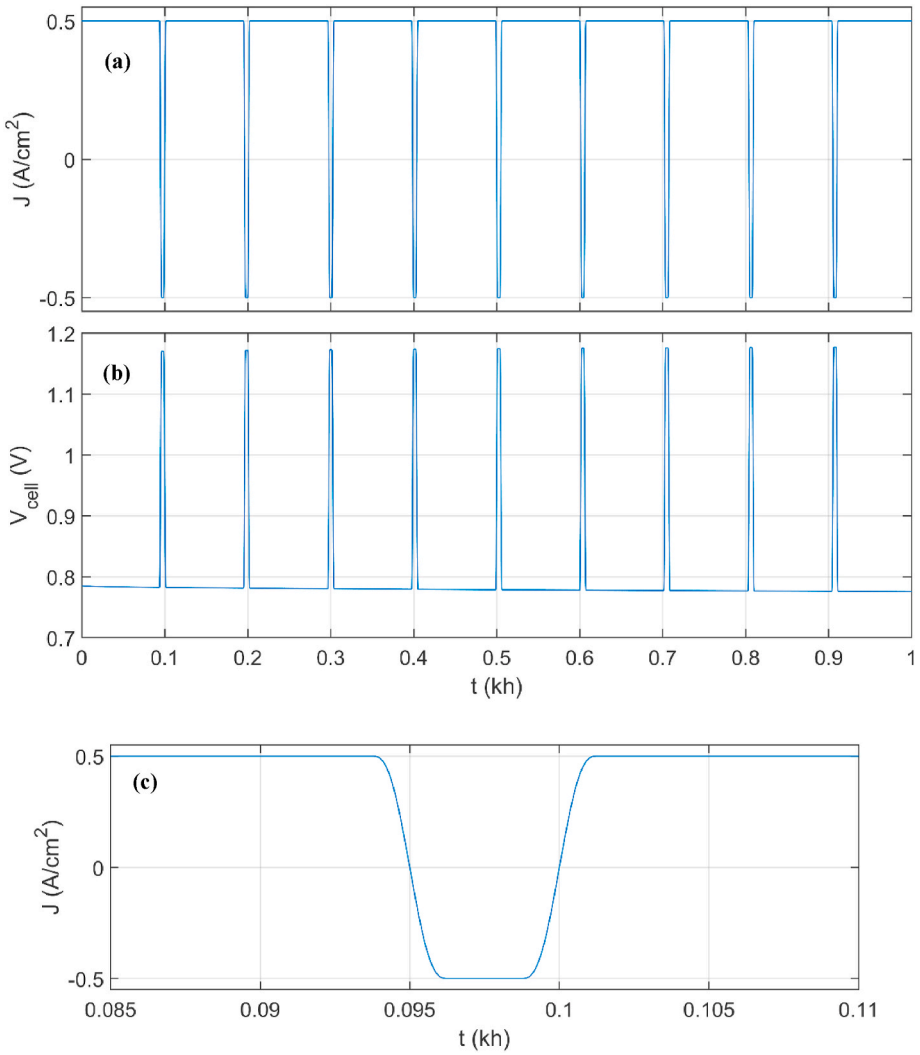

Fig. 2. (a) Pulses used for the load current density under cyclic operation, (b) the resulting cell voltage, and (c) the first load current density cycle.

Table 6
Operating conditions for both SOFC and SOEC operation modes.

Parameter	Value	Description
T_{in}	700 °C	Inflow temperature
p_{out}	101325 Pa	Outlet pressure
$p_{in,fuel}$	102.5 Pa	Fuel inlet gauge pressure
$p_{in,air}$	1700 Pa	Air inlet gauge pressure
J	0.5 A/cm^2	Load current density magnitude for the base operation
$x_{H_2,in}$	0.5	Hydrogen mole fraction at the inlet
$x_{O_2,in}$	0.21	Oxygen mole fraction at the inlet

variables for the base SOFC operation without pulsed cycling of the current density. The variables are the cell voltage and averages of the activation overpotentials of the air and fuel electrodes, Ni particle radius, normalized TPB density of the air and fuel electrodes, electronic conductivity of the fuel electrode, and area-specific-resistance (ASR) of the oxide scale over the interconnect.

The model predicts the common degradation trend of initial decay, linear regime, and a final accelerated regime [17,21], as shown in Fig. 3a. The evolutions for the cell voltage, degradation phenomena, and related model variables illustrated in Fig. 3 are consistent with common trends that have been reported in the literature for constant operating conditions [9,16,21,32,33]. A detailed discussion of the results presented in Fig. 3 can be found in our recent work for a 3D stack model [17].

Comparisons of these 1D model results with the 3D model ones are shown in the Supplementary material. It is shown that the 1D model predicts the same trends as the 3D model but with some discrepancies between them. The models' differences are due to the discrepancies between the modeling variables from the models, especially current density and temperature that are the main modeling variables affecting the degradation models. This is reasonable as the 1D model does not resolve the variations of the modeling variables along the height of the stack.

3.1. Cyclic operations compared to base operation

Fig. 4 shows comparisons of evolutions of the cell voltages under the base (fuel cell) and cyclic operations. The solid-colored fields stem from overlapping lines plotting the vertical shift between SOFC and SOEC mode of operation, which has a high frequency compared to the simulated time scale. The figure legends provide total power productions of the stack over its lifetime, in MWh/cm^2, under the base and cyclic operations. Fig. 4a shows the cyclic operation starting from the beginning, while Fig. 4b shows it starting after 12.5 kh, where the acceleration of the Cr degradation occurs, with the specific electrode simulated in this study. Cr poisoning causes the final accelerated degradation regime [17,21].

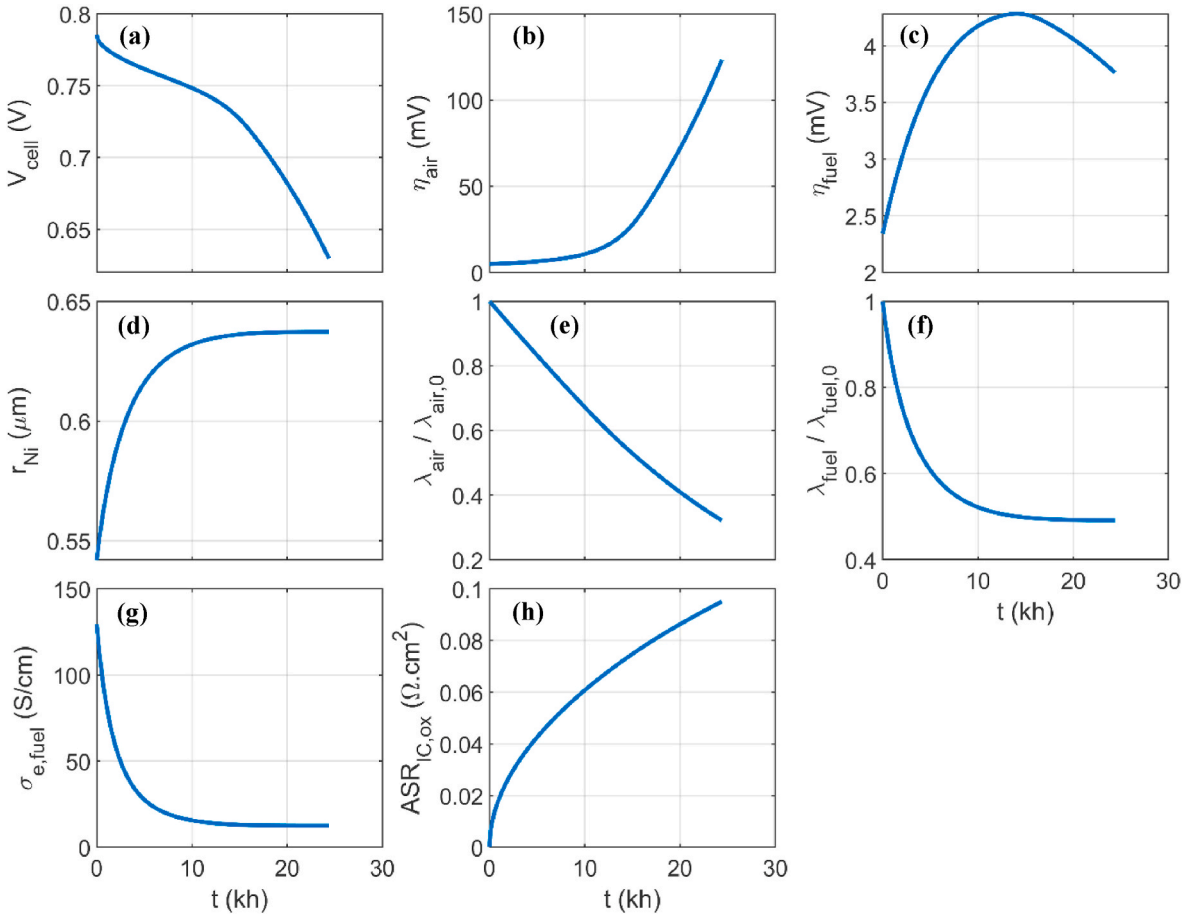

Fig. 3. Evolutions of (a) cell voltage and averages of: (b) activation overpotential of the air electrode, (c) activation overpotential of the fuel electrode, (d) Ni particle radius, (e) normalized TPB density of the air electrode, (f) normalized TPB density of the fuel electrode, (g) electronic conductivity of the fuel electrode, and (h) ASR of the oxide scale over the interconnect.

Fig. 4 indicates that cyclic operations improve the cell lifetime by alleviating the final accelerated degradation regime (Cr poisoning). Therefore, it can be concluded that operating the cell at electrolysis mode can clean the Cr poisoning over the air electrode, which has already been demonstrated in an experimental study by Zhu et al. [28]. The model captures this Cr cleaning under the electrolysis operation mode via the activation overpotential of the air electrode, which is switching to negative values leading to negative reaction rates and so increasing the TPB density of the air electrode, as indicated in Eqs. (24) and (25).

One can see that the cyclic operations enhance the total power production of the stack, which increases with the operating time under the electrolysis mode. For instance, cyclic operations starting from the beginning with 10 and 20% operation time under the electrolysis mode improve the cell lifetime by 36 and 100%, respectively, and the total power production by 19 and 53%, respectively. This demonstrates that the lifetime improvements under the cyclic operations are high enough to compensate for the operation periods under the electrolysis mode.

Fig. 5 shows the effect of the cyclic operation on the activation overpotential of the air electrode. The exponential evolution of the activation overpotential, as illustrated in Fig. 5a, indicates that the degradation of the air electrode contributes to the increased degradation rate. Moreover, this figure shows the alleviating effect of the cyclic operation on the activation overpotential of the air electrode (Cr poisoning), which is due to its negative values under the electrolysis operation mode.

This alleviating effect of the cyclic operation on the activation overpotential of the air electrode can be seen in Fig. 5b for its distributions along the flow direction at 8, 16, and 24 kh. For the base SOFC operation, the activation overpotential increases at the inlet of the active area, where the maximum current density is located, with time to a maximum level and starts to proceed into the active area afterward. However, for the cyclic operation, the maximum value of the activation overpotential is much lower than the base operation and limited to a smaller portion of the active area.

Fig. 6 shows comparisons of evolutions of the cell voltages, total power, and hydrogen production under the base operation and cyclic operations starting from the beginning and after 12.5 kh. To resolve the solid colored fields and make the comparisons clearer, only lower voltages of each cycle, i.e. under fuel cell mode, are shown for the cyclic operations. It is seen that the cyclic operations starting from the beginning result in longer lifetimes and higher total power and hydrogen production over the lifetime than for the base case with the constant fuel cell operation.

The cyclic operations initiated at the beginning show a significantly longer lifetime than the cyclic operations started after 12.5 kh. For

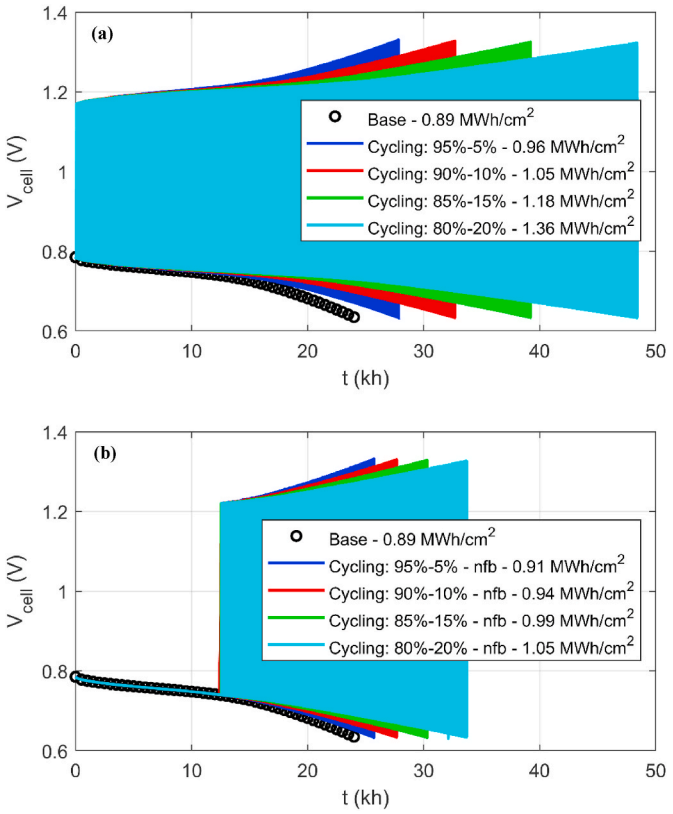

Fig. 4. Comparisons of evolutions of the cell voltages under the base operation (fuel cell) and cyclic operations: (a) starting from the beginning and (b) starting after 12.5 kh. The first number after cycling shows the percentage of operation time at fuel cell mode, and the second number shows the percentage of operation time at electrolysis mode. The last number shows the total power production in MWh/cm^2. The abbreviation nfb represents cyclic operations not conducted from the beginning of the cell lifetime.

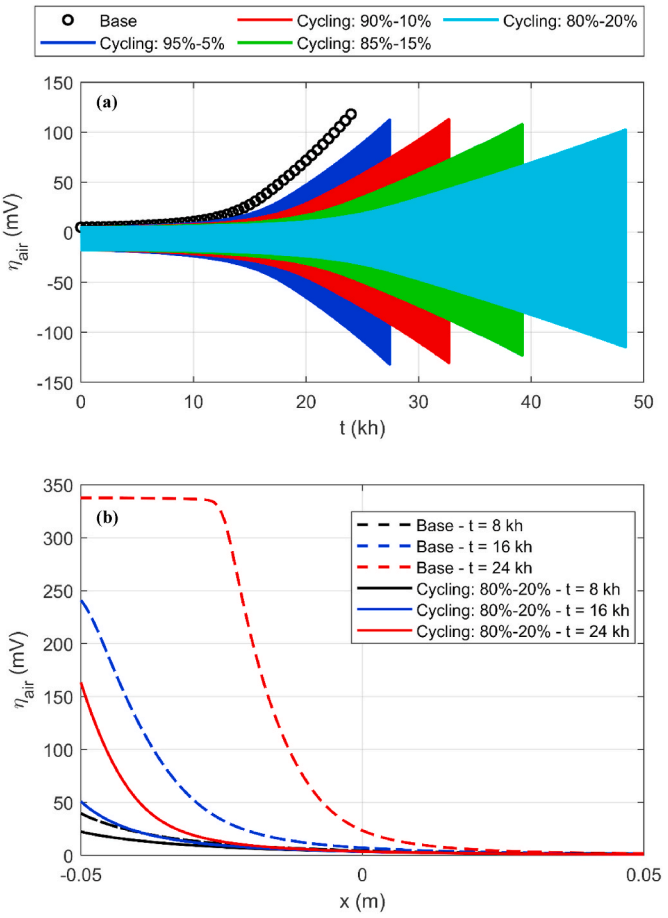

Fig. 5. Comparisons of evolutions of the activation overpotential of the air electrode under the base operation (fuel cell) and cyclic operations starting from the beginning: (a) averages of the activation overpotentials over the cell lifetime, and (b) distributions of the activation overpotentials along the active area at 8, 16, and 24 kh.

instance, cyclic operations with 20% operation time under the electrolysis mode starting from the beginning and after a certain period improve the cell lifetime by 100 and 40%, respectively, and the total power production by 53 and 18%, respectively. Therefore, the cyclic operation should be started from the beginning to clean the Cr poisoning continuously and prevent its accumulation over the TPBs.

3.2. Effects of the fuel cell and electrolysis current densities on the cyclic operation

Fig. 7 shows the effects of the base load current densities on the evolutions of the cell voltages, total power, and hydrogen production under the base operations and cyclic operations starting from the beginning with 20% operation time under electrolysis mode. Again, it is seen that the cyclic operation improves the lifetime and total power output as compared to the constant base operation for different load current densities. Both base and cyclic operations show similar trends of shorter lifetime and higher total power production for higher load current density.

Interestingly, the rate of the total power improvement for higher load current densities and lifetime improvement for lower load current densities are almost the same for both base and cyclic operations. Hence, the cyclic operation behavior with the load current density is similar to that of the common fuel cell operation. Moreover, the ratios of the lifetimes and total powers of the cyclic and base operations are close for all the load current densities; these ratios are slightly higher for the load current density of 0.4 A/cm^2.

Finally, the effects of the electrolysis current density on the cyclic operation are investigated, as shown in Fig. 8. Electrolysis current densities of −0.25, −0.5 (base), and −0.8 A/cm^2 are considered, and the time fraction of each operation mode is adjusted so that it results in equivalent hydrogen production for each cycle. It has to be noted that a fixed load current density of 0.5 A/cm^2 is used for the fuel cell mode.

Fig. 8 shows that the cyclic operation with a lower electrolysis current density (/longer operation time under the electrolysis mode) has the longest lifetime and highest total power and hydrogen production. This indicates that the duration of the electrolysis mode is more effective than the magnitude of the negative activation overpotential in cleaning the Cr poisoning. This outcome leads to more benefits as the lower current densities ensure that the cell does not significantly degrade during the electrolysis operation mode; this is important as the cell degrades faster under electrolysis mode than the fuel cell mode. However, the same alleviation has been shown for the degradation phenomena occurring under electrolysis mode by the cyclic operation to the fuel cell mode [27].

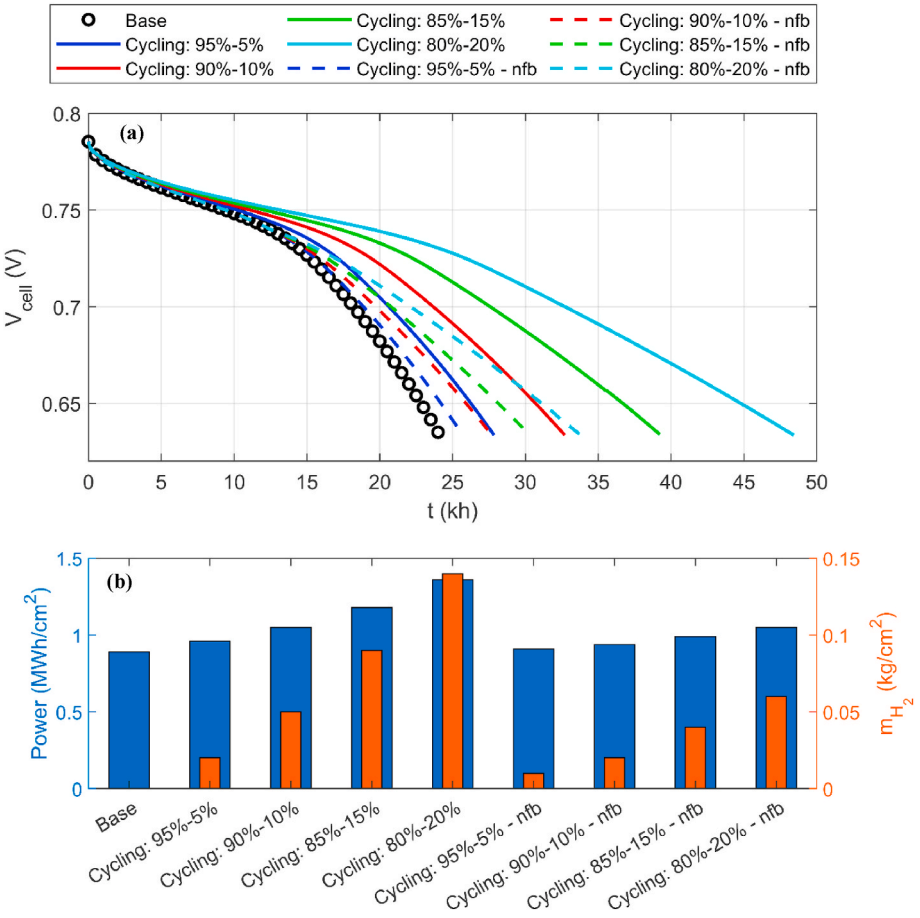

Fig. 6. Comparisons of the base operation (fuel cell) and cyclic operations: (a) evolutions of the cell voltages, and (b) total power and hydrogen production over the lifetime of the stack. Solid and dashed lines show the lower voltages for the cyclic operation starting from the beginning and after 12.5 kh, respectively.

4. Discussion

In a power grid, ancillary services are required by the transmission service operator (TSO) to maintain the integrity and stability of the transmission and distribution system and the power quality. Some of the ancillary services are traded on electricity markets, while other ancillary services such as short-circuit power, inertia, reactive reserves, and voltage control are not traded on the market. The TSO may instead choose to advertise the procurement of these services at different notices and durations.

The increasing electricity production from wind and solar power increases the requirement for ancillary services to mitigate unforeseen imbalances between power production and consumption. Dynamically operated SOFC systems that also can be operated as electrolysers for hydrogen production, as the one considered in the current paper, can provide such services. The co-production of ancillary services can generate substantial revenues for the service provider.

The system for the reverse operation of the SOC would be more complex (/expensive) than the one used for the common operation of the SOCs as it needs more elaborate control strategies to adapt the inlets and outlets for each operation mode, e.g. the stack taking hydrogen from a tank under the fuel cell mode, while supplying hydrogen to the tank under the electrolysis mode.

The current study shows that the reverse operation of the SOC alleviates the Cr poisoning of the air electrode occurring under fuel cell operation mode and so enhances the lifetime of the SOC stack. The longer lifetime leads to higher outputs from the stack both in terms of power and hydrogen production. Therefore, this higher stack output together with the benefits of the ancillary services for the reverse operation, could overcome the expenses of making the system compatible with such a reverse operation. These first investigations of the potential lifetime increase open up to a techno-economic study of the potential gains.

Our results show that the reversed pulse operation with longer operation times under electrolysis mode, starting from the beginning, and having lower electrolysis current densities improve the cell lifetime, total power, and hydrogen production notably. However, a maximum of 20% of the cycle time is considered for the electrolysis operation in this study as the degradation phenomena, especially Ni migration, occurring under the electrolysis mode are not included. Nonetheless, the degradation phenomena under electrolysis mode could be alleviated by cyclic to the fuel cell mode [27].

Future studies will be performed with a more elaborated model, e.g. with updated Cr poisoning model for newer air electrode materials such as LSCF, including different rates for Cr poisoning and cleaning, and adding the Cr poising through chemical reactions, which are neglected for the SOFC operation as their rates are negligible compared to the Cr poisoning via the electrochemical reaction; however, their effects could be comparable having the electrochemical cleaning of the chromium.

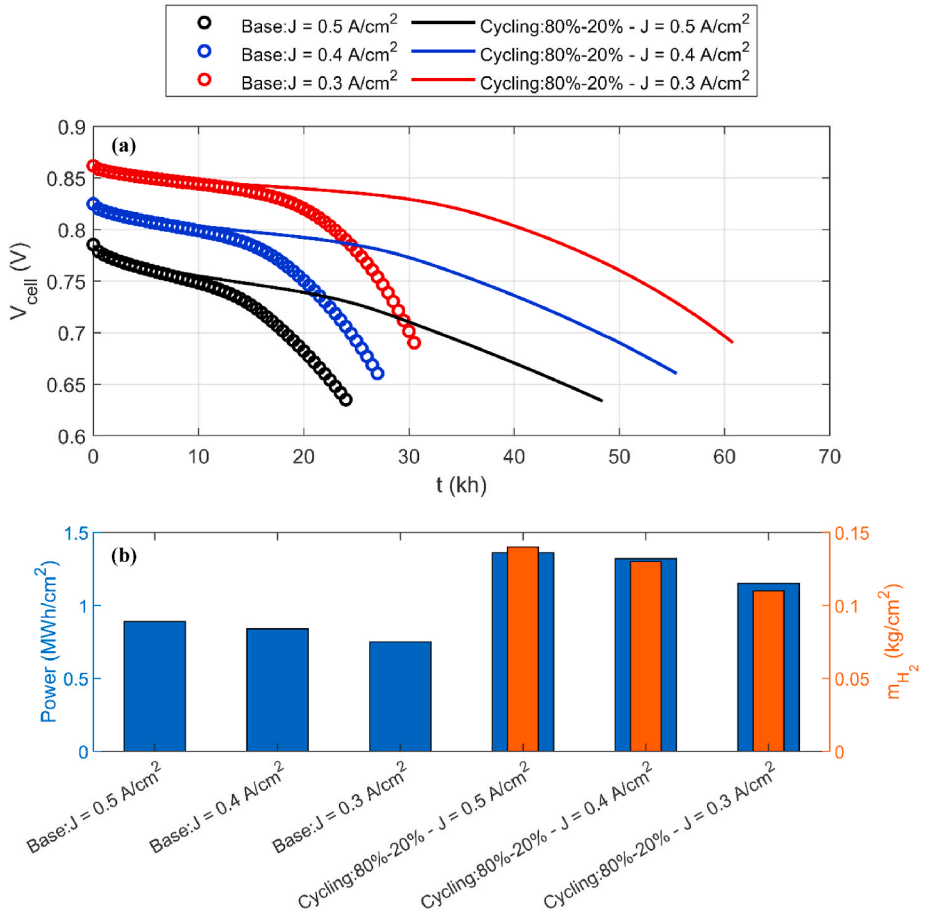

Fig. 7. Comparisons of the base operation (fuel cell) and cyclic operations starting from the beginning with 20% operation time under electrolysis mode for different base load current densities: (a) evolutions of the cell voltages, and (b) total power and hydrogen production over the lifetime of the stack.

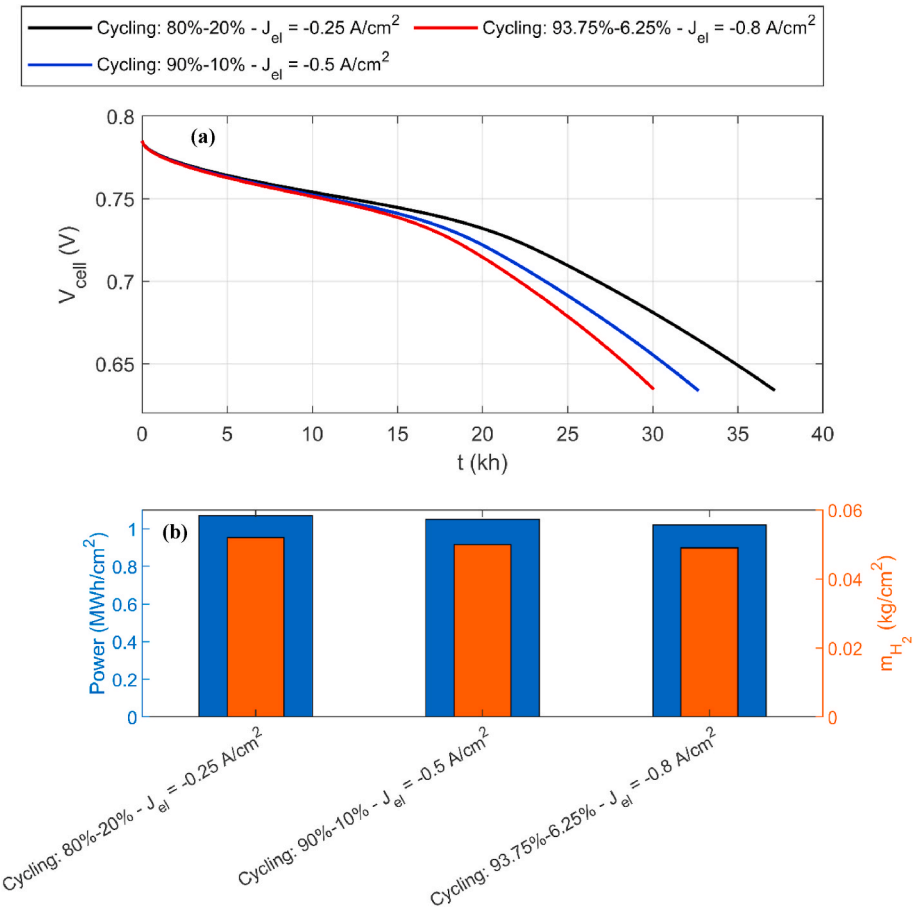

Fig. 8. Comparisons of the cyclic operations starting from the beginning for different electrolysis current densities: (a) evolutions of the cell voltages, and (b) total power and hydrogen production over the lifetime of the stack.

Moreover, the Ni coarsening model needs to be updated as the current model developed by Ref. [9], which is one of the most recent and thorough models developed for the Ni coarsening, is not impacted by changes in overpotential and gas composition induced by the cyclic operation, as shown in Fig. 3 of the Supplementary material. Furthermore, the increased chance of mechanical failure due to the higher temporal and spatial temperature gradients over the stack can also be a challenge from the dynamic operation suggested here. However, new tougher cells, sealings, and contact layers are constantly developed for the SOC stack to withstand the dynamic operation better. Such a mechanical analysis can be done by integrating the stack-scale mechanical model [31] with a 3D degradation model [17].

The model will be used to study the effects of the reversible cyclic operation on other degradation phenomena occurring under both fuel cell and electrolysis modes. We expect further improvements in the SOC performance since alleviating effect of the reversed pulse operation on other degradation phenomena has been recently demonstrated in experimental studies in the literature. Furthermore, such a thorough model, including the effects of the reversed operation on other degradation phenomena as well, such as Ni migration, will be used for a system-level economic analysis comparing the benefits of the reverse operation mode on the stack outputs, i.e. power and hydrogen, and the extra expenses that are necessary for running the stack under the reverse operation.

5. Conclusion

In this study, a multiphysics model of an SOC is used to investigate the effects of reversed pulse operation on alleviating Cr poisoning. We show how the Cr poisoning model used in this study captures the alleviation of the Cr poisoning of the modeled LSM/YSZ air electrode. Moreover, the effects of the time fraction of the operation under fuel cell and electrolysis modes, cyclic operation not starting from the beginning, and fuel cell and electrolysis current densities on the lifetime, total power, and hydrogen production of the SOC are investigated. The reversible cyclic operations considered in this study improve the lifetime and total power production of the stack. The model predicts that the cyclic operation starting from the beginning with a 20% operation time under the electrolysis mode improves the cell lifetime and total power production by 100 and 53%, respectively.

Results indicate that the cyclic operation starting after a certain period is not as effective as the cyclic operation starting from the beginning in enhancing the cell performance (cell lifetime, total power, and hydrogen production). Moreover, longer operation times under electrolysis mode extend the lifetime of the cells. Furthermore, it is found that different fuel cell current densities lead to almost the same improvements in the cell performance, while lower electrolysis current densities with higher operation times enhance the cell performance.

The results presented in this study are based on a model including degradation phenomena of Ni coarsening, Cr poisoning of the LSM/YSZ electrode, and IC oxidation. The results are influenced by the Cr poisoning model for the LSM/YSZ electrode, and using newer air electrode materials such as LSCF would quantitatively but not qualitatively lead to different results. Also, including other degradation phenomena such as Ni migration, which is a major one under SOEC operation mode, would result in a more accurate representation of both operations when such models are available. Similar alleviating effects of the cyclic operation on the other degradation phenomena are expected as they

have already been shown in recent experimental studies.

CRediT authorship contribution statement

Omid Babaie Rizvandi: Conceptualization, Methodology, Software, Investigation, Writing – original draft, Visualization. **Søren Højgaard Jensen:** Conceptualization, Methodology, Writing – review & editing. **Henrik Lund Frandsen:** Supervision, Conceptualization, Methodology, Writing – review & editing, Project administration, Funding acquisition.

Declaration of competing interest

The authors declare that they have no known competing financial interests or personal relationships that could have appeared to influence the work reported in this paper.

Acknowledgments

The research leading to these results was funded by the project "Energy system modelling using digital twins for future technologies" financed by DTU-Energy. The funding is gratefully acknowledged.

Appendix A. Supplementary data

Supplementary data to this article can be found online at https://doi.org/10.1016/j.jpowsour.2022.231048.

References

[1] I. Sreedhar, B. Agarwal, P. Goyal, A. Agarwal, An overview of degradation in solid oxide fuel cells-potential clean power sources, J. Solid State Electrochem. 24 (2020) 1239–1270.
[2] M.S. Sohal, J.E. O'Brien, C.M. Stoots, V.I. Sharma, B. Yildiz, A. Virkar, Degradation issues in solid oxide cells during high temperature electrolysis, J. Fuel Cell Sci. Technol. 9 (1) (2012).
[3] R. Knibbe, A. Hauch, J. Hjelm, S.D. Ebbesen, M. Mogensen, Durability of Solid Oxide Cells, 2011.
[4] Y. Wang, W. Li, L. Ma, W. Li, X. Liu, Degradation of solid oxide electrolysis cells: phenomena, mechanisms, and emerging mitigation strategies—a review, J. Mater. Sci. Technol. 55 (2020) 35–55.
[5] K. Chen, Materials degradation of solid oxide electrolysis cells, J. Electrochem. Soc. 163 (11) (2016) F3070.
[6] P. Moçoteguy, A. Brisse, A review and comprehensive analysis of degradation mechanisms of solid oxide electrolysis cells, Int. J. Hydrogen Energy 38 (36) (2013) 15887–15902.
[7] S.P. Jiang, J.P. Zhang, L. Apateanu, K. Foger, Deposition of chromium species at Sr-doped LaMnO3 electrodes in solid oxide fuel cells. I. Mechanism and kinetics, J. Electrochem. Soc. 147 (11) (2000) 4013.
[8] J.J. Bentzen, J.V.T. Høgh, R. Barfod, A. Hagen, Chromium poisoning of LSM/YSZ and LSCF/CGO composite cathodes, Fuel Cell. 9 (6) (2009) 823–832.
[9] J. Zhu, Z. Lin, Degradations of the electrochemical performance of solid oxide fuel cell induced by material microstructure evolutions, Appl. Energy 231 (2018) 22–28.
[10] J.G. Maillard, Development of Modelling and Testing for Analysis of Degradation of Ni-YSZ Anode in Solid Oxide Fuel Cells, Doctoral dissertation, University of Birmingham, 2018.
[11] M. Keane, M.K. Mahapatra, A. Verma, P. Singh, LSM–YSZ interactions and anode delamination in solid oxide electrolysis cells, Int. J. Hydrogen Energy 37 (22) (2012) 16776–16785.
[12] M.B. Mogensen, A. Hauch, X. Sun, M. Chen, Y. Tao, S.D. Ebbesen, P.V. Hendriksen, Relation between Ni particle shape change and Ni migration in Ni–YSZ electrodes–a hypothesis, Fuel Cell. 17 (4) (2017) 434–441.
[13] Z. Yang, K.S. Weil, D.M. Paxton, J.W. Stevenson, Selection and evaluation of heat-resistant alloys for SOFC interconnect applications, J. Electrochem. Soc. 150 (9) (2003) A1188–A1201.
[14] D. Larrain, D. Favrat, Simulation of SOFC stack and repeat elements including interconnect degradation and anode reoxidation risk, J. Power Sources 161 (1) (2006) 392–403.
[15] A. Hagen, R. Barfod, P.V. Hendriksen, Y.L. Liu, S. Ramousse, Degradation of anode supported SOFCs as a function of temperature and current load, J. Electrochem. Soc. 153 (6) (2006) A1165–A1171.
[16] K. Miyoshi, H. Iwai, M. Kishimoto, M. Saito, H. Yoshida, Chromium poisoning in (La, Sr) MnO3 cathode: three-dimensional simulation of a solid oxide fuel cell, J. Power Sources 326 (2016) 331–340.
[17] O.B. Rizvandi, X.Y. Miao, H.L. Frandsen, Multiscale modeling of degradation of full solid oxide fuel cell stacks, Int. J. Hydrogen Energy 46 (2021) 27709–27730.
[18] E. Konysheva, H. Penkalla, E. Wessel, J. Mertens, U. Seeling, L. Singheiser, K. Hilpert, Chromium poisoning of perovskite cathodes by the ODS alloy Cr5Fe1Y2O3 and the high chromium ferritic steel Crofer22APU, J. Electrochem. Soc. 153 (4) (2006) A765–A773.
[19] E. Konysheva, J. Mertens, H. Penkalla, L. Singheiser, K. Hilpert, Chromium poisoning of the porous composite cathode effect of cathode thickness and current density, J. Electrochem. Soc. 154 (12) (2007) B1252–B1264.
[20] T. Horita, D.H. Cho, F. Wang, T. Shimonosono, H. Kishimoto, K. Yamaji, et al., Correlation between degradation of cathode performance and chromium concentration in (La, Sr) MnO3 cathode, Solid State Ionics 225 (2012) 151–156.
[21] A. Nakajo, P. Tanasini, S. Diethelm, D. Favrat, Electrochemical model of solid oxide fuel cell for simulation at the stack scale II: implementation of degradation processes, J. Electrochem. Soc. 158 (9) (2011) B1102–B1118.
[22] X. Chen, Chromium deposition and poisoning of cathodes of solid oxide fuel cells–a review, Int. J. Hydrogen Energy 39 (1) (2014) 505–531.
[23] Z. Sun, R. Wang, A.Y. Nikiforov, S. Gopalan, U.B. Pal, S.N. Basu, CuMn1. 8O4 protective coatings on metallic interconnects for prevention of Cr-poisoning in solid oxide fuel cells, J. Power Sources 378 (2018) 125–133.
[24] D.M. Bierschenk, J.R. Wilson, S.A. Barnett, High efficiency electrical energy storage using a methane–oxygen solid oxide cell, Energy Environ. Sci. 4 (3) (2011) 944–951.
[25] V. Venkataraman, M. Pérez-Fortes, L. Wang, Y.S. Hajimolana, C. Boigues-Muñoz, A. Agostini, P.V. Aravind, Reversible solid oxide systems for energy and chemical applications–review & perspectives, J. Energy Storage 24 (2019) 100782.
[26] G.A. Hughes, K. Yakal-Kremski, S.A. Barnett, Life testing of LSM–YSZ composite electrodes under reversing-current operation, Phys. Chem. Chem. Phys. 15 (40) (2013) 17257–17262.
[27] C. Graves, S.D. Ebbesen, S.H. Jensen, S.B. Simonsen, M.B. Mogensen, Eliminating degradation in solid oxide electrochemical cells by reversible operation, Nat. Mater. 14 (2) (2015) 239–244.
[28] Z. Zhu, M. Sugimoto, U. Pal, S. Gopalan, S. Basu, Electrochemical cleaning: an in-Situ method to reverse chromium poisoning in solid oxide fuel cell cathodes, J. Power Sources 471 (2020) 228474.
[29] A. Hauch, S.D. Ebbesen, S.H. Jensen, M. Mogensen, Solid oxide electrolysis cells: microstructure and degradation of the Ni/yttria-stabilized zirconia electrode, J. Electrochem. Soc. 155 (11) (2008) B1184.
[30] M. Navasa, X.Y. Miao, H.L. Frandsen, A fully-homogenized multiphysics model for a reversible solid oxide cell stack, Int. J. Hydrogen Energy 44 (41) (2019) 23330–23347.
[31] X.Y. Miao, O.B. Rizvandi, M. Navasa, H.L. Frandsen, Modelling of local mechanical failures in solid oxide cell stacks, Appl. Energy 293 (2021) 116901.
[32] L.G.J. De Haart, J. Mougin, O. Posdziech, J. Kiviaho, N.H. Menzler, Stack degradation in dependence of operation parameters; the real-SOFC sensitivity analysis, Fuel Cell. 9 (6) (2009) 794–804.
[33] A. Nakajo, F. Mueller, J. Brouwer, D. Favrat, Progressive activation of degradation processes in solid oxide fuel cell stacks: Part II: spatial distribution of the degradation, J. Power Sources 216 (2012) 434–448.
[34] M. Navasa, X.Y. Miao, H.L. Frandsen, A fully-homogenized multiphysics model for a reversible solid oxide cell stack, Int. J. Hydrogen Energy 44 (41) (2019) 23330–23347.
[35] T. Kawada, N. Sakai, H. Yokokawa, M. Dokiya, M. Mori, T. Iwata, Characteristics of slurry-coated nickel zirconia cermet anodes for solid oxide fuel cells, J. Electrochem. Soc. 137 (10) (1990) 3042.
[36] S. Nagata, A. Momma, T. Kato, Y. Kasuga, Numerical analysis of output characteristics of tubular SOFC with internal reformer, J. Power Sources 101 (1) (2001) 60–71.
[37] Y. Suzue, N. Shikazono, N. Kasagi, Micro modeling of solid oxide fuel cell anode based on stochastic reconstruction, J. Power Sources 184 (1) (2008) 52–59.
[38] K. Miyoshi, T. Miyamae, H. Iwai, M. Saito, M. Kishimoto, H. Yoshida, Exchange current model for (La0. 8Sr0. 2) 0.95 MnO3 (LSM) porous cathode for solid oxide fuel cells, J. Power Sources 315 (2016) 63–69.
[39] A. Leonide, Y. Apel, E. Ivers-Tiffee, SOFC modeling and parameter identification by means of impedance spectroscopy, ECS Trans. 19 (20) (2009) 81.
[40] W. Kong, J. Li, S. Liu, Z. Lin, The influence of interconnect ribs on the performance of planar solid oxide fuel cell and formulae for optimal rib sizes, J. Power Sources 204 (2012) 106–115.
[41] R.T. Nishida, S.B. Beale, J.G. Pharoah, Comprehensive computational fluid dynamics model of solid oxide fuel cell stacks, Int. J. Hydrogen Energy 41 (45) (2016) 20592–20605.
[42] M. Kvesić, U. Reimer, D. Froning, L. Lüke, W. Lehnert, D. Stolten, 3D modeling of a 200 cm2 HT-PEFC short stack, Int. J. Hydrogen Energy 37 (3) (2012) 2430–2439.
[43] S. Gao, J. Li, Z. Lin, Theoretical model for surface diffusion driven Ni-particle agglomeration in anode of solid oxide fuel cell, J. Power Sources 255 (2014) 144–150.
[44] R.T. Nishida, S.B. Beale, J.G. Pharoah, L.G.J. de Haart, L. Blum, Three-dimensional computational fluid dynamics modelling and experimental validation of the Jülich Mark-F solid oxide fuel cell stack, J. Power Sources 373 (2018) 203–210.